Outflow in global magnetohydrodynamics as a function of a passive inner boundary source

D. T. Welling[1] and M. W. Liemohn[1]

[1]Department of Atmospheric, Oceanic, and Space Sciences, University of Michigan, Ann Arbor, Michigan, USA

Abstract Numerous studies of the terrestrial magnetosphere that use global magnetohydrodynamic codes have found that the model's inner boundary can act as a significant source of plasma, even if the radial velocity about the boundary is held at zero. Though inherent in many models, this "de facto outflow" is poorly understood. This work uses the Block Adaptive Tree Solar Wind Roe-type Upwind Scheme MHD model to investigate the behavior of this type of outflow as a function of boundary conditions and solar wind drivers. It is found that even for temporally and spatially constant boundary conditions, the mass is accelerated away from the body in a dynamic manner. Fluxes organize into cusp, polar cap, and auroral zone concentrations. Pressure gradient forces appear predominantly responsible for cusp and polar cap outflow, while the Lorentz force, resulting from field-aligned current systems, is the strongest driver of outflow in other regions. Integrated fluxes probed just outside of the inner boundary vary linearly as a function of cross polar cap potential and solar wind dynamic pressure. The resulting dynamics strongly resemble patterns found in in situ measurements, while net fluences agree within an order of magnitude. Two free parameters, inner boundary mass density and composition, can strongly affect results. Accounting for these unknowns is likely best left to physics-based or empirical specifications of outflow. Despite this, such outflow appears to be an acceptable proxy.

1. Introduction

Including an ionospheric source of magnetospheric plasma into a global magnetohydrodynamic (MHD) model is an exercise in prescribing inner boundary conditions (IBCs): outflowing plasma is generated by setting a density and radial velocity at some geocentric radius (typically 2.5 to 3.0 R_E). This can be done in an artificial manner, i.e., imposing preselected conditions to drive outflow for a tightly controlled experiment [e.g., *Garcia et al.*, 2010; *Wiltberger et al.*, 2010; *Yu and Ridley*, 2013]. Alternatively, advanced approaches have been developed to set IBCs in a dynamic manner. This has been done using empirical relationships [e.g., *Gagne*, 2005; *Damiano et al.*, 2010; *Brambles et al.*, 2010, 2011; *Ouellette et al.*, 2013] and first-principles-based methods [e.g., *Glocer et al.*, 2009a, 2009b; *Welling et al.*, 2011]. In any case, these changes to the IBCs are motivated by the need to include the ionospheric source of magnetospheric plasma, which plays a key role in magnetospheric dynamics [e.g., *Lennartsson and Shelley*, 1986; *Chappell et al.*, 1987; *Moore and Delcourt*, 1995; *Daglis et al.*, 1999; *Denton et al.*, 2005].

The goal behind the various IBC applications is to capture the magnetosphere-ionosphere relationships that accelerate H^+ and O^+ from low-altitude source regions to magnetospheric altitudes. It has been known for a long time that ambipolar outflow of light ions to supersonic velocities (i.e., the "classical" polar wind [*Axford*, 1968; *Banks and Holzer*, 1968; *Ganguli*, 1996]) is an ever-present acceleration mechanism. While this process can deliver O^+ ions to very high altitudes, they remain gravitationally bound unless other processes, such as wave-particle interactions [e.g., *Chaston et al.*, 2004, 2007], centrifugal acceleration [e.g., *Cladis*, 1986; *Horwitz et al.*, 1994], and affects of hot electron populations [e.g., *Barakat and Schunk*, 1983; *Barakat et al.*, 1998], provide further acceleration. This so-called "generalized" polar wind can contribute a significant amount of O^+ to the magnetosphere. Accurately including these fluxes in global MHD models is paramount to accurately modeling the magnetosphere.

Welling and Ridley [2010a], investigating paths of solar wind plasma (upstream boundary) and ionospheric plasma (inner boundary) through the magnetosphere, differed from the above studies by not specifying outflow explicitly. Rather, the default IBCs for the Block Adaptive Tree Solar Wind Roe-type Upwind Scheme (BATS-R-US) global MHD model were used: constant mass density and zero radial velocity. With these very
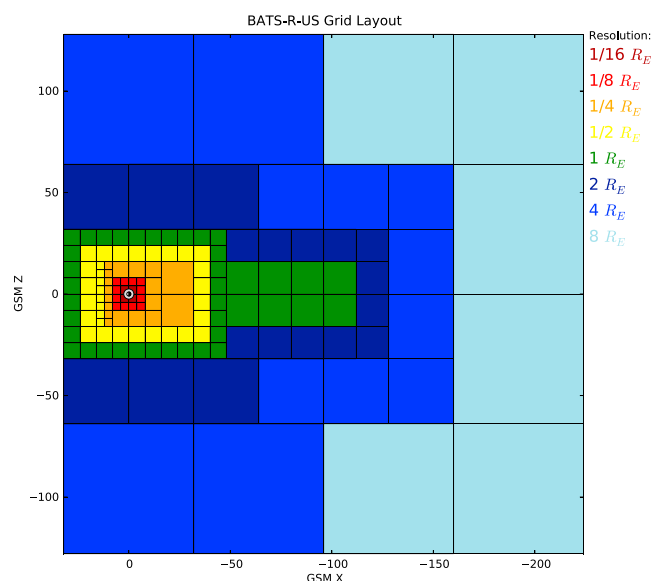
Figure 1. The resolution used in this study across the equatorial plane. Colored areas indicate regions of uniform cell size. The grid layout is symmetric such that a slice taken from the noon-midnight meridian plane would appear identical to this slice.

simple settings, plasma originating from the inner boundary dominated results within the inner magnetosphere and plasma sheet during southward interplanetary magnetic field (IMF) configurations. Similarly, *Zhang et al.* [2007] found that inner boundary-originating mass contributed to the ring current development and that the inner boundary (IB) density controlled the strength of this contribution. This behavior is not isolated to BATS-R-US. Using a different single-fluid MHD model with similar IBCs, *Walker et al.* [2003] demonstrated that the inner boundary of their model acts as a passive source of plasma. Their results closely resembled those obtained by *Siscoe et al.* [2001] using an independently developed MHD code. The multifluid model of *Winglee* [1998] has relied on such inner boundary effects to determine the boundary between regions dominated by ionospheric origin or solar wind-origin plasma, map heavy ion outflows into the greater magnetosphere [*Winglee*, 2000], and investigate how these outflows affect the cross polar cap potential (CPCP) [*Winglee et al.*, 2002]. It is apparent that for a set of IBCs, the MHD inner boundary provides *de facto outflow*, i.e., outflow that arises "in practice but not necessarily ordained by law." This behavior is not alarming, as it plays the role of ionospheric outflow, which can provide the preponderance of magnetospheric mass in the real ionosphere-magnetosphere system [e.g., *Horwitz*, 1987; *Chappell et al.*, 1987; *Nosé et al.*, 2003].

To a great extent, this proxy remains poorly understood. Do de facto outflow fluxes at all resemble their real-world counterparts? Are there temporal or spatial dynamics, or is inner boundary mass a simple, static reservoir that diffuses radially outward uniformly? Does this source vary with upstream conditions? Initial progress has been made in previous studies by estimating the total fluence (i.e., spatially integrated flux) entering the MHD domain [*Walker et al.*, 2003; *Winglee*, 2000]. *Winglee et al.* [2008] performed initial quiet-time data-model flux comparisons, but simulation fluxes were obtained from five Earth radii (R_E) and mapped down to ionospheric altitudes. Outflow mechanisms are either not addressed in these previous studies or were evaluated using external particle tracing codes [e.g., *Winglee*, 2003]. This work addresses these questions to put previous studies in proper context and inform future investigations that include this important effect.

2. Methodology

This work leverages the single-fluid version of the BATS-R-US MHD model [*Powell et al.*, 1999; *De Zeeuw et al.*, 2000]. This model has a strong history of terrestrial magnetosphere investigations [*Gombosi et al.*, 1998; *Ridley et al.*, 2002; *Tóth et al.*, 2007; *Zhang et al.*, 2007] and validation [*Yu and Ridley*, 2008; *Wang et al.*, 2008; *Welling and Ridley*, 2010b]. It uses an adaptive Cartesian grid in the Geocentric Solar Magnetospheric (GSM) coordinate system. For this study, the inner boundary is set to a sphere of radius 2.5 R_E; the outer boundary is 32 R_E in the upstream direction, 224 R_E downstream, and 128 R_E in each other direction. For this study, idealized solar wind and interplanetary magnetic field (IMF) values are imposed as the upstream boundary conditions. On inner boundary cell faces, mass density (ρ) and radial velocity (V_R) remain fixed in space and time. The default values for these are 28 amu/cm^3 and 0, respectively. In this study, V_R is never changed. Velocity tangent to the inner boundary is set using electric potential values from a coupled, height-integrated ionospheric electrodynamics solver [*Ridley and Liemohn*, 2002; *Ridley et al.*, 2004]. To simplify interpretation of the results of this study, the dipole is set parallel to the planetary spin axis.
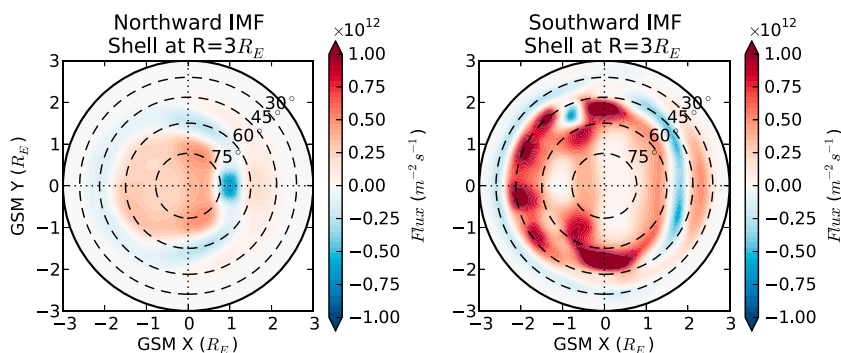
Figure 2. Radial particle fluence (assuming an all-hydrogen plasma) passing through a sphere of $3\,R_E$. Only the Northern Hemisphere is shown; the sun would be to the right of each plot. (left) Pseudo-steady state conditions during northward IMF and (right) results during southward IMF conditions. Degrees shown are latitudes on the shell; if a dipole field is assumed, the rings at 75°, 60°, 45°, and 30° map to magnetic invariant latitudes 81°, 73°, 66°, and 60°, respectively.

Inherent in all numerical models is an aspect of numerical diffusion; steps are taken in this work and others to reduce the impact on results. The Rusanov solver [*Rusanov*, 1961] is used with a mixing of the minmod (robust but diffusive) and monotonized central (MC, nondiffusive but less stable) flux limiters. Blending the two reduces diffusion but retains model robustness. As numerical diffusion is proportional to grid cell size, high spatial resolution is used in this study, especially toward the inner boundary and related regions of interest. The smallest cell size has a width of $1/16\,R_E$. A total of 7.9 million computational cells was used for each simulation. The resolution layout is illustrated in Figure 1. Finally, the "Boris correction" factor [*Boris*, 1970; *Gombosi et al.*, 2002] is employed to artificially reduce the speed of light by a factor of 50. In semirelativistic MHD, this slows the maximum wave speed, thus increasing the minimum time step. Because numerical diffusion is dependent on the maximum wave speed in the simulation [*Powell et al.*, 1999; *Lyon et al.*, 2004], the Boris factor inhibits diffusion as well. All of these methods work to reduce the diffusion in the simulations presented here.

Using this setup, a series of idealized simulations is performed. Upstream earthward velocity and plasma temperature are kept constant at 450 km/s and 10.34 eV (120,000 K), respectively, for all simulations. Upstream $V_{Y,Z}$ and $B_{X,Y}$ (GSM coordinates) are set to zero for all simulations. A variety of interplanetary B_Z and solar wind number density values are selected throughout the study to investigate outflow patterns and dependence on key upstream parameters. Whenever values change midsimulation, they change quickly and are then held constant for at least 5 h in order to reach a pseudo-steady state, simplifying the interpretation of the results. All analysis and visualization is performed using the Spacepy software library [*Morley et al.*, 2010].

3. Results

3.1. Characteristics and Behavior

The first simulation examines the characteristics of de facto outflow by first holding interplanetary B_Z at 3 nT for 5 h, then flipping southward to a value of −10 nT for 5 h. Default inner boundary (IB) density was used. This first simulation acts as a baseline against which to compare the others.

Figure 2 shows the radial number flux, assuming an all-hydrogen plasma, passing through a sphere of $3\,R_E$, merely $1/2\,R_E$ and eight computational cells away from the inner boundary. Latitude shown is latitude on the shell; if a dipole field is assumed, the rings at 75°, 60°, 45°, and 30° map to magnetic invariant latitudes 81°, 73°, 66°, and 60°, respectively. Even at this short distance from the inner boundary, the outflowing mass has formed interesting patterns. Note that the fluxes shown in Figure 2 are those at the $3\,R_E$ shell and have not been mapped to the ionosphere or some other reference altitude. During northward interplanetary magnetic field conditions (Figure 2, left), outflowing fluxes (red contours) are relegated to the poleward regions. Precipitation (downward fluxes, i.e., blue contours) occurs strongly around the cusp region and surrounding the polar cap. During southward IMF conditions (Figure 2, right), the area of outflowing plasma increases dramatically. At the midlatitude dayside (right side of plot between 30° and 45° magnetic latitude), moderate upflow is observed. Moving poleward, this is followed by moderate downflow, then a wide area of weak to moderate upflow. Between the 45° and 60° latitude markers, there are two upflowing intensity peaks, one
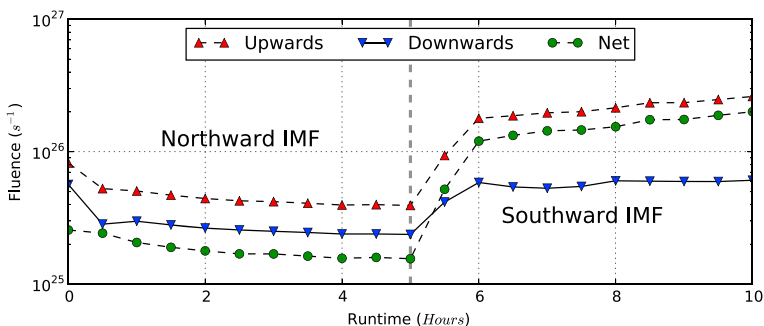
Figure 3. Fluence through the Northern Hemisphere of a sphere of radius 3 R_E. Upward fluence is denoted by upward facing red triangles, downward fluence by downward facing blue triangles, and net fluence by green circles. The southward turning of the IMF occurs 5 h into the simulation and is denoted by the vertical dashed gray line.

dawn-centered and one dusk-centered. Centered at 45° and midnight is a broad region of strong upflow, followed by weaker downflow at lower latitudes. This figure shows that de facto outflow is activity dependent and is organized into regions that roughly correspond to cusp, polar cap, and auroral zone outflow, even when the IBCs are spatially uniform. These results are mirrored symmetrically in the Southern Hemisphere (not shown).

To examine the total ion contribution from the inner boundary, the flux is integrated across the surface of the 3 R_E sphere to yield a total particle fluence. Again, an all H$^+$ plasma is assumed. The results versus simulation time are shown in Figure 3. During northward IMF conditions, the net fluence is on the order of 10^{25} ions/s (Figure 3, green circles, left of the vertical dashed line). After a transition period that lasts approximately 1 h, the fluence increases by an order of magnitude. Fluence is roughly conserved when this calculation is repeated at subsequent altitudes (not shown). This further demonstrates that the amount of outflowing plasma varies strongly with activity even when the inner boundary conditions are held constant.

A rough estimate of how much each spatial region contributes to the total fluence can be made by dividing the hemisphere into equal quadrants and integrating the quadrant fluxes into quadrant fluences. The four quadrants each span 90° longitude and are centered about magnetic local time (MLT) noon, dusk, midnight, and dawn. Figure 4 shows this comparison for upward fluences, normalized to total upward fluence. Reproducing this calculation for net fluence produces qualitatively congruent results. During southward IMF conditions, the dawn and dusk quadrants each account for ~25% of the upward fluences. The noon quadrant contributes the least (15–20%), while the night side contributes the most (30%). Well after the southward turning, this pattern has not changed much with the exception of a dawn-dusk asymmetry that favors the dawn side (up to 25%) over the dusk (20% and dropping). Immediately after the southward turning, there is a transition period where the noon-centered quadrant becomes the dominant region (35%) at the expense of the others. This pattern changes quickly, with the preturning ordering of each quadrant restored 3 h after the IMF rotation. Though simple, this analysis demonstrates the high regional variability of de facto-type outflow.

But how does this outflow arise? Figure 5 outlines the progression of three separate fluid parcels originating at different points about
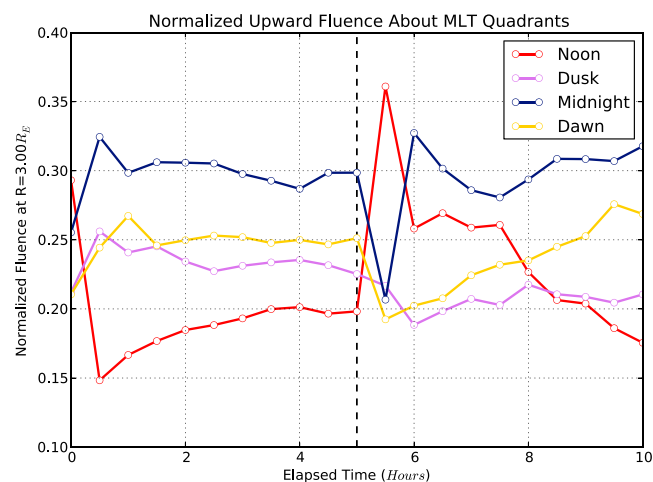

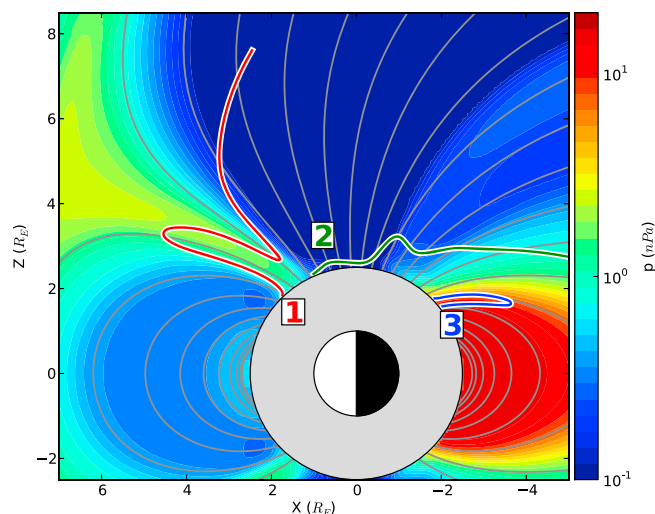
Figure 4. Upward fluences for four 90° wide quadrants: noon, dusk, midnight, and dawn. Each is normalized by the total upward fluence. The southward turning of the IMF occurs 5 h into the simulation and is denoted by the vertical dashed line.

Figure 5. Streamline traces of three fluid parcels originating at different inner boundary latitudes and flowing through the GSM $Y = 0$ plane. The Earth is represented by the black and white circle (colors denote day and night sides), and the inner boundary is denoted by the gray circle. Gray lines mark a sample of the terrestrial magnetic field lines. The color contour is the plasma thermal pressure.

the inner boundary and accelerating into the greater domain. The paths were generated by integrating the fluid streamlines during the southward IMF, pseudo-steady state portion of the baseline simulation. Streamline 1 (red) shows the path taken by a parcel originating near-cusp, streamline 2 (green) shows the path of one originating in the polar cap, and streamline 3 (blue) is of one starting near the nightside auroral zone. The color bar shows contours of constant pressure and illustrates one of the key forces involved in accelerating the parcels: gradient pressure force.

Starting at the IB footpoint of any of the three, it is apparent that the outflow mechanisms are initially numerical: numerical diffusion allows mass to enter the computational domain from the inner boundary cell faces, even though the radial velocity at the cell faces is set to zero. No other process allows for this entry as V_{normal} at the boundary cell face is set to zero. This process manifests even here, where numerical diffusion is strongly limited by both high resolution at the inner boundary ($1/16\,R_E$) and use of the Boris speed-of-light factor. Because of this diffusion, the inner boundary essentially acts as a mass reservoir for the greater domain.

It is important to emphasize that though the diffusion of mass into the computational domain is numerical in nature, this does not mean that it is unphysical. At the inner boundary, the density, velocity, and temperature represent moments of a Maxwellian distribution. Even though the bulk motion of the fluid is zero, half of the distribution has a positive radial component of its random velocity, so we would expect it to enter the computational domain of the model.

Though numerical diffusion allows the mass to enter the computational domain, the MHD equations quickly take over to accelerate the mass into the greater magnetosphere. Returning to Figure 5, all three streamlines are accelerated away from the body and into the domain. Streamlines 1 (red) and 3 (blue) start on stronger pressure gradients, so they move outward more quickly. Streamline 2 (green) lies in a region of weak pressure gradient forces but strong $\bar{E} \times \bar{B}$ drift, as set by the ionospheric electrodynamic model. This parcel moves immediately antisunward until nightside pressure gradients push it further outward. Parcels 1 and 3 eventually encounter earthward pressure gradient forces and reverse direction. For streamline 3, this is due to the more energetic ring current population suppressing outward flow; the parcel ultimately precipitates into the inner boundary. Meanwhile, streamline 1 has reached an equilibrium with inflowing plasma of solar wind origin, driving it back down. Because this simulation was performed in the single-fluid MHD limit, the solar wind and ionospheric populations cannot counterstream in the cusp region. The local convection of magnetic field lines eventually pulls the streamline 1 parcel out of the cusp and toward the lobes. The pressure gradient force is again pointing radially outward and drives the parcel into the magnetosphere.

Of course, pressure gradients are not the only force acting on near-boundary populations. Figure 6 shows the force densities for the baseline simulation over a sphere of radius $3\,R_E$ (eight computational cells away from the inner boundary): radial pressure gradient (Figure 6, top), Lorentz force (Figure 6, middle), and the sum of the two (Figure 6, bottom). Purple regions denote radially inward oriented forces; orange regions indicate upward forces. It should be noted that the radial Lorentz forces arise in regions where field-aligned-currents are expected but from the portion of the current that is not field-aligned. While there are more sophisticated ways to describe the forces at work (e.g., as the ponderomotive force arising
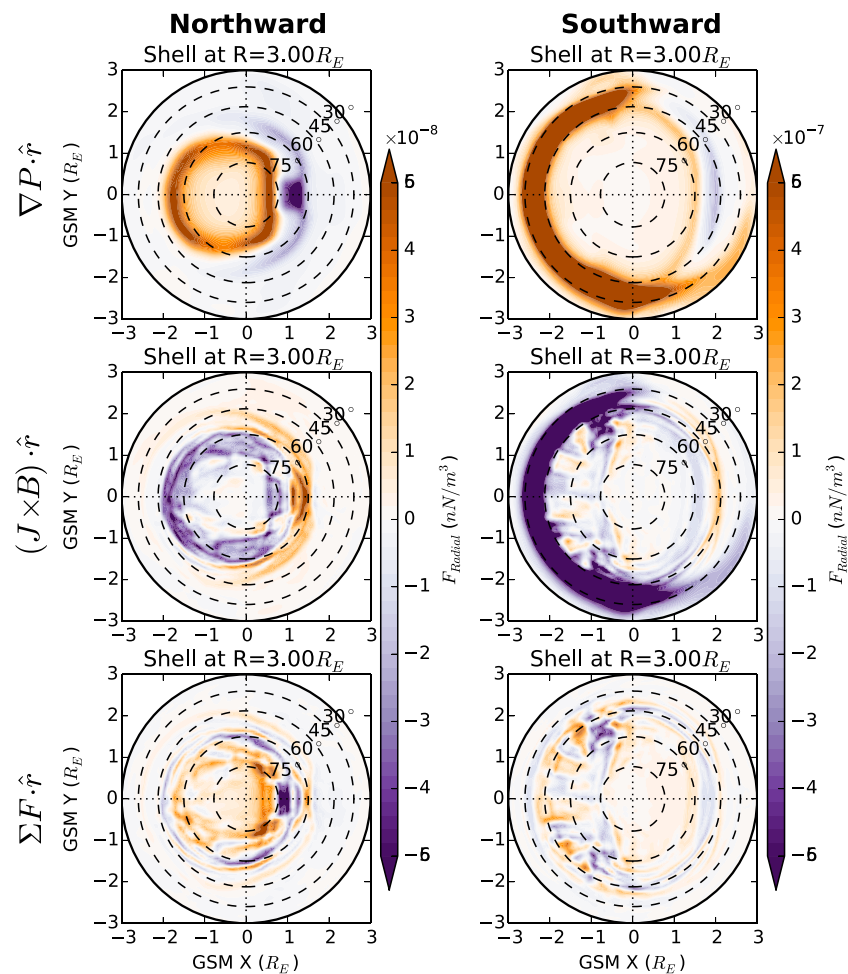
Figure 6. Force density maps about a sphere of radius 3 R_E for (left column) northward IMF (right column) and southward IMF. The force density resulting from (top) pressure gradient force, (middle) $J \times B$ force, and (bottom) the sum of the two are shown. Note that the color bars have different scales (by a factor of 10) for each column.

from Alfven waves [*Guglielmi et al.*, 1996]), such an analysis is beyond the scope of this initial study. During northward IMF conditions, electromagnetic and pressure gradient forces combine to create an "up-down-up" sequence, ordered from low to high latitudes. This force pattern matches the flux pattern shown in Figure 2 (left). At higher latitudes, gradient pressure forces overwhelm the Lorentz force and drive polar cap outflow. During southward IMF conditions (right), the situation becomes more complicated. The dayside has changed from exhibiting a well-pronounced cusp during northward IMF to a broader acceleration region, yet it retains the "up-down-up" force pattern. Continuing poleward, pressure gradient forces continue to drive polar cap outflows. Between 30 and 45° latitude on the nightside, gradient pressure and Lorentz forces nearly balance each other out perfectly. At slightly higher latitudes, detailed currents, associated with dynamics in the plasma sheet and inner magnetosphere, drive complex force patterns, explaining the more nuanced flux patterns observed in the right frame of Figure 2. With increasing (decreasing) altitude, the force magnitudes diminish (grow) and the features spread to lower (higher) latitudes, but the overall patterns remain roughly fixed (not shown).

3.2. Dependence on Inner Boundary Density

Inner boundary density changes the rate of diffusion and sets the depth of the reservoir. To illustrate, the above experiment was repeated for four different inner boundary densities: 0.1, 5, 50, and 500 amu/cm³. The resulting fluences are compared against the baseline case (28 amu/cm³) in Figure 7. The results are clearly ordered and mimic the patterns of the baseline results. Using a least squares fitting to a power law,
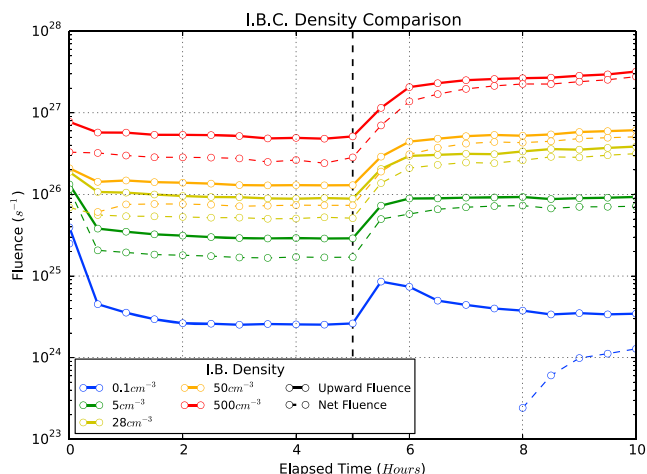
Figure 7. Total fluence for five different inner boundary mass densities spanning 3 orders of magnitude. Upward fluence is denoted by the solid lines, net fluence denoted by dashed lines. Negative net values are not displayed. The southward turning of the IMF occurs 5 h into the simulation and is denoted by the vertical dashed line.

the net fluence at the end of the simulation (J_{net}) is related to the inner boundary density (ρ) by the following expression:

$$J_{net} = (1.295 \times 10^{25})\rho^{0.911} \qquad (1)$$

The units of the constant are $s^{-1}(cm^3/amu)^{0.911}$, and the units of the other factors remain the same as before.

The result for 0.1 amu/cm³ (Figure 7, blue lines) stands out from the rest. Omitting a short-lived jump, the upward fluence does not notably increase from northward to southward IMF conditions. Furthermore, the net fluence does not become positive until nearly 8 h into the simulation. In other words, the predominant behavior for this choice of

IB density is precipitation, not outflow. De facto outflow is clearly controlled by the inner boundary mass reservoir and can even be effectively "shut off" when ρ is set to low enough values.

3.3. Dependence on Solar Drivers

Given the variable forces and resultant fluxes, it is clear that de facto outflow dynamics are tied tightly to upstream conditions. To investigate these relationships, a third set of simulations is performed where a specific value, either IMF B_Z or solar wind dynamic pressure (P_{dyn}), is varied in stepwise fashion. After each step, the upstream values are held constant for 5 h so that the magnetosphere can adjust to the new activity. The inner boundary density remains at the baseline value of 28 amu/cm³ throughout each of these simulations.

3.3.1. Interplanetary Magnetic Field

Figure 8 summarizes the results when IMF B_Z is stepped from +10 to −20 nT in 5 nT increments over 35 h. Each region of constant IMF is shaded differently for reference. The net fluence (again taken from a shell of radius 3 R_E) increases somewhat during the first 15 h but then rapidly increases as IMF turns southward. Eventually, this value saturates near 3.5×10^{26} s⁻¹. Meanwhile, the smoothed CPCP (solid green line) begins with a value around 20 kV, drops as IMF B_Z drops to 5 nT, then increases as IMF B_Z is reduced to near zero.
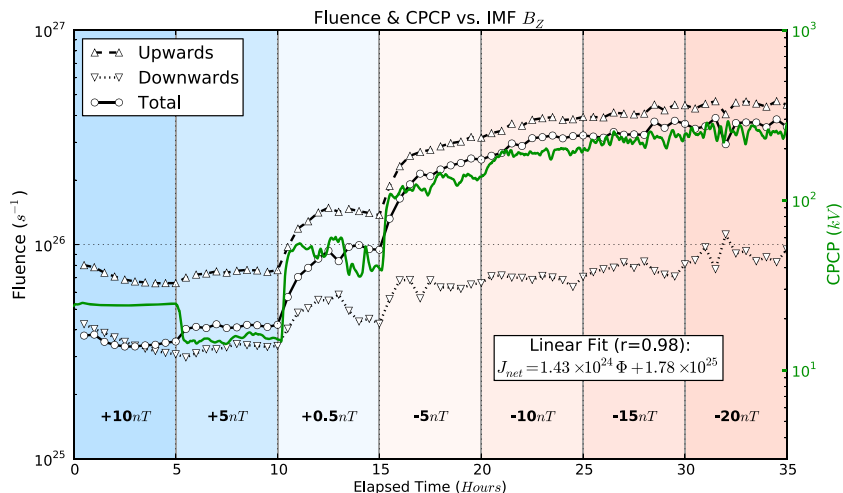

Figure 8. Upward (upward triangles), downward (downward triangles), and net (circles) fluences and cross polar cap potential (green line) versus simulation time and IMF B_Z. Periods of constant IMF are shaded different colors.
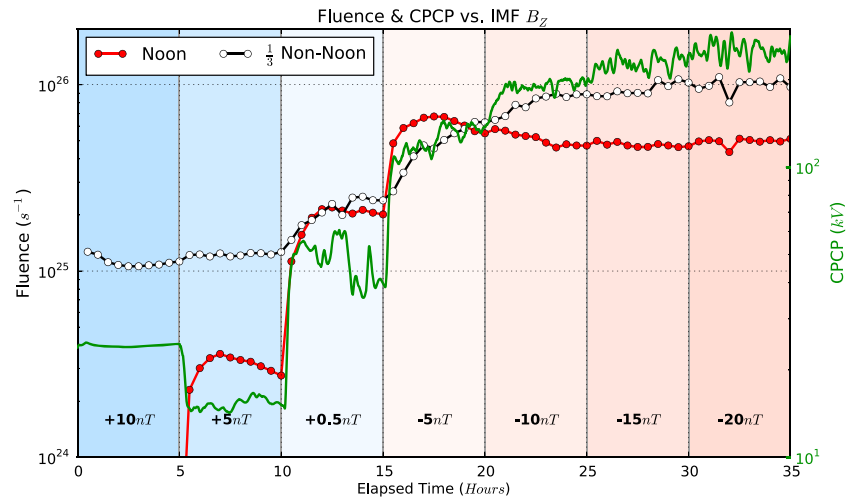
Figure 9. Similar to Figure 8 but showing net fluence from the noon-centered quadrant only (red line) and the average fluence from all other quadrants (black line).

This increase is the result of reverse convection patterns, driven by the northward IMF B_Z (NBZ) current system [*Burke et al.*, 1979], no longer shielding forward convection patterns, which are constantly driven by flank viscous interactions [*Axford and Hines*, 1961]. Subsequently, the cross polar cap potential (CPCP, smooth green line) continues to grow until it saturates around 200 kV. This behavior mirrors the net fluence closely; the only exception is during the first 5 h of the simulation where reverse convection potentials surpass those from viscous interactions about the flanks. A simple linear regression yields the following relationship between net fluence (J_{net}) and CPCP (Φ):

$$J_{net} = (1.43 \times 10^{24})\Phi_{CPCP} + 1.78 \times 10^{25} \qquad (2)$$

The units of the first and second constants are $s^{-1}\,kV^{-1}$ and s^{-1}, respectively. This relationship correlates strongly with the results, with a correlation coefficient of 0.98. The calculation of the coefficient includes 71 points and is statistically significant to the 99% confidence interval. Clearly, de facto fluxes are closely related to magnetospheric activity.

The relationship between IMF B_Z and de facto outflow is further explored in Figures 9 and 10. Figure 9 splits the net upward fluence shown in Figure 8 into net fluence originating from the noon-centered quadrant (red line) and the average fluence from the three other quadrants (black line). During the first half of the
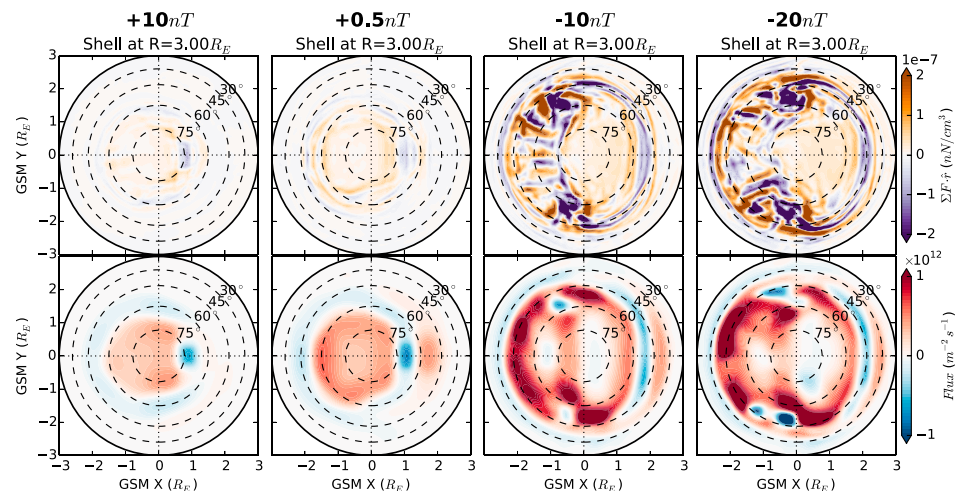

Figure 10. (top) Net radial force density and (bottom) the associated net particle flux taken at the end of four different IMF B_Z steps: +10, +0.5, −10, and −20 nT (first to fourth columns, respectively).
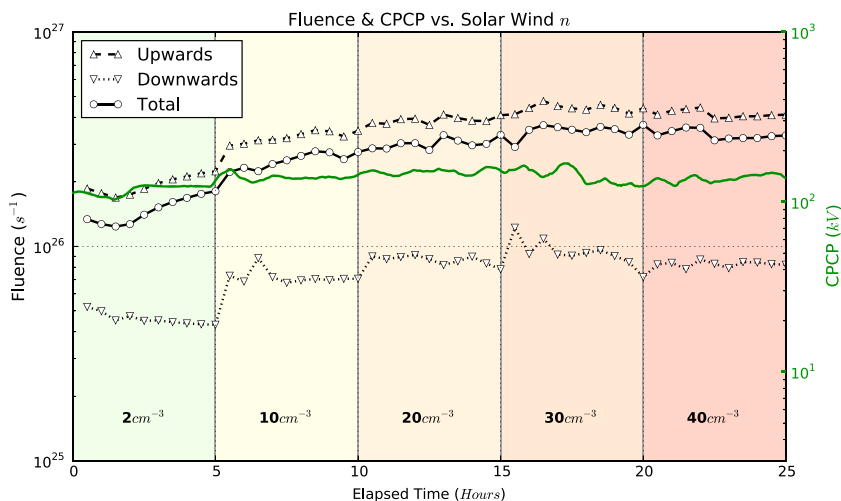
Figure 11. Similar to Figure 8 but when solar wind proton density is varied (therefore, P_{dyn}) instead of IMF B_Z. Periods of constant number density are shaded different colors.

simulation, the noon-centered outflow dynamics mirror the CPCP, while the other quadrants remain relatively flat. As IMF B_Z transitions from northward to near zero to southward, the correlation is handed from the dayside outflow to the flanks and nightside. During the final half of the simulation, the noon-centered contribution remains near-constant, while fluence from the rest of the MLT sectors continues to increase with CPCP. Figure 10 illustrates the same feature in terms of net radial force density (Figure 10, top) and the associated fluxes (Figure 10, bottom). Early in the simulation (Figure 10, first column), nightside $\bar{J} \times \bar{B}$ forces are limited as the NBZ current system shields the forward convection system created by viscous interactions. As IMF B_Z decreases, $\bar{J} \times \bar{B}$ forces on the dayside begin to increase (Figure 10, second column), increasing dayside flux contributions. A moderate amount of magnetospheric pressure can build up as the activity increases, increasing flux contributions from the other MLT sectors. During strongly southward IMF B_Z conditions (Figure 10, third and fourth columns), net dayside forces increase only marginally, limiting the acceleration from this region. In all other regions, however, current densities and pressure gradients increase substantially, driving strong outflows in those quadrants.
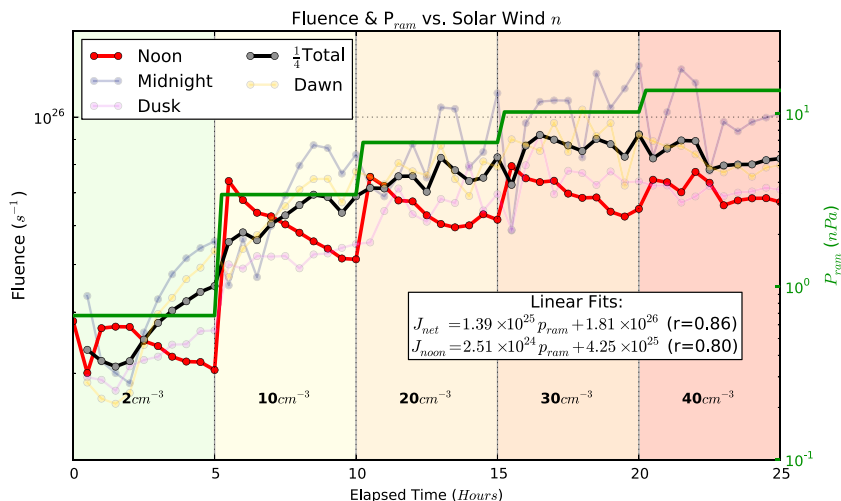

Figure 12. Fluence values plotted against simulation time. Total fluence (black line) is divided by 4 to gather all lines on a reasonable scale. Fluence from the noon-centered MLT quadrant is in red; other quadrants are shown as semitransparent lines. Regions of constant upstream proton density are shaded in different colors. The solid green line shows the upstream dynamic pressure.
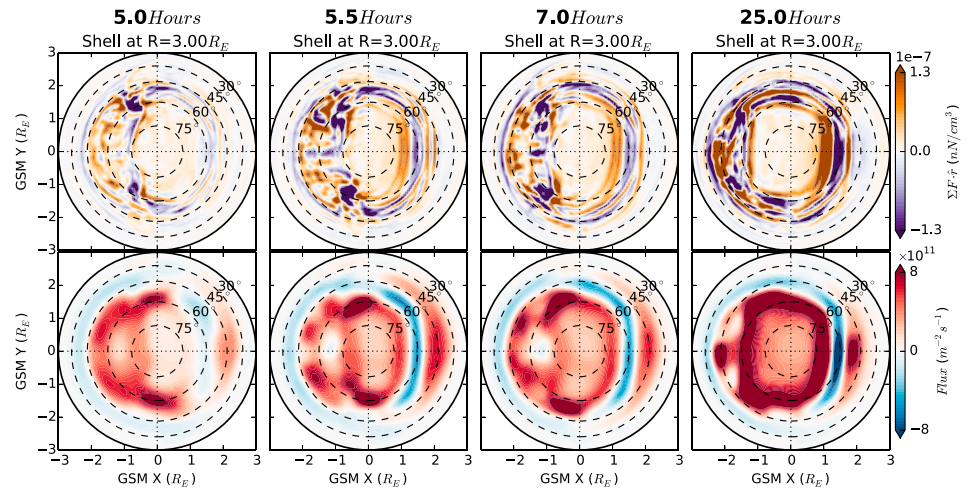
Figure 13. Similar to Figure 10 but for four separate epochs during the variable P_{dyn} simulation. Columns correspond to 5, 5.5, 7, and 25 h simulation time.

3.3.2. Solar Wind Dynamic Pressure

The final simulation turns from the effects of IMF B_Z to the effects of solar wind dynamic pressure. Similar to the previous simulation, P_{dyn} is varied by changing upstream proton number density in stepwise fashion from 2 cm^{-3} to 40 cm^{-3} over 25 h. Solar wind velocity and IMF are held constant at 450 km/s and −5 nT, respectively, to drive a baseline level of activity.

Figure 11 summarizes the results in a similar fashion to Figure 8. For this case, however, there does not appear to be a clear relationship between CPCP and the net upward fluence. While both do increase over the course of the simulation, CPCP does so very weakly. If a linear regression is performed as was done before, the resulting correlation coefficient is only 0.588, indicating a weak relationship.

Figure 12 casts the results in a clearer form by comparing the resulting fluences against P_{dyn} (solid green line) instead of CPCP. Additionally, fluences from each MLT quadrant are included, and the net fluence (black line) is divided by 4 to keep all lines on a convenient scale. This arrangement makes the relationship between outflowing fluxes and P_{dyn} clearer. As P_{dyn} steps upward, the total net fluence slowly grows and appears to saturate toward the end of the simulation, albeit in a noisy fashion. A linear regression between the total net fluence (J_{net}) and P_{dyn} yields

$$J_{net} = (1.39 \times 10^{25})P_{dyn} + 1.81 \times 10^{26} \tag{3}$$

The units of the first and second constants are s^{-1} nPa^{-1} and s^{-1}, respectively. The correlation coefficient for this relationship is 0.86, signifying strong correlation. The coefficient is calculated using 51 points and is statistically significant to the 99% confidence interval. Of the four MLT quadrants, the noon sector net fluence (J_{noon}, red line) stands out as responding quickly and sharply to each impulse then decaying before the next. Other quadrants (semitransparent lines) roughly follow the slow growth trend of the total fluence. At higher P_{dyn} values, the response of the noon sector becomes weaker and the fluence appears to saturate. A linear regression that focuses on this sector exclusively yields

$$J_{net,noon} = (2.51 \times 10^{24})P_{dyn} + 4.25 \times 10^{25} \tag{4}$$

The units of the first and second constants are s^{-1} nPa^{-1} and s^{-1}, respectively. This relationship does not correlate as strongly as that of J_{net}, with a coefficient of 0.80. The coefficient is calculated using 51 points and is statistically significant to the 99% confidence interval. P_{dyn} appears to have two effects: slow, cumulative growth of J_{net} and impulsive growth on J_{noon}.

Figure 13 illustrates the dynamics that drive the results shown in Figure 12. Similar to Figure 10, Figure 13 (top) shows the net force density at four separate epochs; Figure 13 (bottom) shows the corresponding net fluxes. Figure 13 (first column) is taken at 5 h simulation time, just as the first pressure impulse is arriving. Dayside radial forces and fluxes are both relatively weak compared to the nightside. Figure 13 (second

column) shows the conditions immediately after the impulse. Overall forces and fluxes are increased, disproportionately on the dayside. After an additional hour and a half (Figure 13, third column), the noon-centered values have subsided marginally, but the forces remained elevated elsewhere. Late in the simulation (Figure 13, fourth column), when dynamic pressure has been held at 13.58 nPa for 5 h, the force density and fluxes are globally increased. The progression here is relatively intuitive. During the impulse, the cusp plasma pressure increases drastically, driving stronger pressure gradients about the cusp near the inner boundary (Figure 5). As the magnetosphere adjusts to the new drivers, this subsides somewhat. Part of this adjustment is an increase in CPCP and additional mass entry into the magnetosphere from the solar wind [see *Welling and Ridley*, 2010a], driving strong tail dynamics, buildup of inner magnetosphere pressure, and, therefore, increased current density. This activity drives stronger, more persistent outflow in the nonnoon quadrants. Through these processes, de facto outflow becomes a function of upstream density and velocity.

4. Relation to Observations

The outstanding question concerning outflow arising from a static, passive inner boundary specification ("de facto") is its veracity: how well does this plasma source resemble observations of ionospheric outflow? Answering this question is challenging given the difficulty of measuring outflow and the limited observational set with which to work. Given that de facto outflow is the default behavior for many MHD models, validation is especially important.

A first-order evaluation can be made by comparing the total fluence against previous numerical studies and observational estimations. Using the baseline IB density of 28 amu/cm^3 and assuming an all-proton plasma, the baseline net hemispheric fluences calculated from this study ranged from 3.35×10^{25} to 3.89×10^{26} ions/s. Increasing the IB density to 500 amu/cm^3 drove values to 2.41×10^{26} and 2.77×10^{27} ions/s; lowering IB density could induce net precipitation instead of outflow. Doubling these values yields the global contribution because of interhemispheric symmetry. These values are on the order of those created by other global models, such as *Winglee* [1998, 2000] (6×10^{26} to 2×10^{27} ions/s for an inner boundary density of 400 ions/cm^{-3}) or *Walker et al.* [2003] (3×10^{26} ions/s for southward IMF and an unspecified boundary density). All of these results compare favorably with estimates from the DE-1 spacecraft, which range from 10^{25} to 10^{26} ions/s [*Yau et al.*, 1988]. Similar ranges have been reported based on Akebono [*Cully et al.*, 2003] and POLAR [*Moore et al.*, 1997] observations.

Magnitudes aside, de facto outflow strongly reproduces expected fluence dynamics. Observed outflow fluences have been shown to correlate strongly with the activity index, K_P [*Yau et al.*, 1988], solar wind electric field and IMF magnitude [*Cully et al.*, 2003], and IMF B_Z polarity [*Lennartsson et al.*, 2004]. Here it is found that de facto fluence correlates strongly with CPCP, which is well known to be tied strongly to upstream parameters [e.g., *Boynton et al.*, 2011, and references therein]. Similarly, relationships between upstream dynamic pressure and outflow fluences have been found both for event studies [e.g., *Moore et al.*, 1999] and on a statistical basis [e.g., *Cully et al.*, 2003; *Lennartsson et al.*, 2004]. De facto outflow has demonstrated an ability to reproduce impulsive increases related to pressure pulses and enduring increases as P_{dyn} remains elevated. Indeed, the response of the dayside de facto fluxes to P_{dyn} is reminiscent of results obtained when an empirically enforced outflow is used [*Damiano et al.*, 2010]. In terms of outflow dynamics, it appears that the de facto approach is qualitatively competitive with more advanced outflow specifications.

5. Discussion and Conclusions

Mass outflow arising from simple MHD inner boundary conditions (i.e., constant mass density and zero radial velocity at all locations), or de facto outflow, is an important and dynamic source of magnetospheric plasma. This outflow manifests even with zero radial velocity about the MHD inner boundary because numerical diffusion allows the boundary to act as a mass reservoir for the greater domain. Once in the first computational cell, MHD pressure gradient and electromagnetic forces accelerate the plasma into the magnetosphere. The net fluence shows a strong linear relationship with CPCP and solar wind dynamic pressure. These dynamics resemble trends identified from observations of outflowing ions. Further, the model-derived fluences agree within an order of magnitude with estimations from observations and other MHD models that applied similar boundary conditions.

The above comparisons to observations lose significance, however, when the free parameters are taken under consideration. Foremost is inner boundary density, which represents the number of ions made
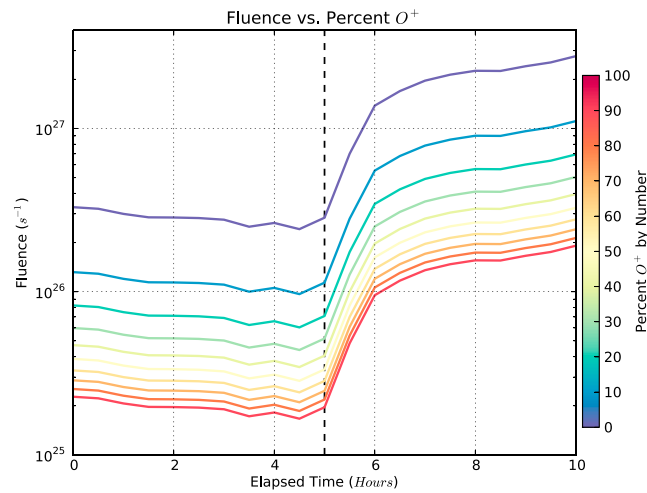
Figure 14. Illustration of how total fluence is impacted as composition changes the total number density in a single-fluid or multispecies MHD paradigm. Fluence is calculated at a shell of $3\,R_E$ geocentric distance when the IB mass density is $500\,amu/cm^3$. The color of each line corresponds to the percent O^+ by number.

available to the magnetosphere from ionospheric upwelling. A spatially and temporally static IB, as is used here, is a poor model for complex ionospheric processes [see *Yau and André*, 1997, and references therein], and Figure 7 demonstrates the strong dependence of net fluence on this value.

Compounding this uncertainty is the issue of composition. The MHD state variable of interest is mass density, not number density. For this study, and many others using single-fluid MHD, an all-proton plasma is assumed. As a larger fraction of the population is assumed to be O^+ while mass density is held constant, the total ion number density falls as

$$n_{\text{total}} = \frac{\rho}{m_{\text{proton}}\left(1 + 15R_{O^+}\right)} \tag{5}$$

where ρ is the total fluid mass density and R_{O^+} is the ratio of oxygen number density to the total (n_{total}). Figure 14 illustrates the impact of increasing R_{O^+} on the net hemispheric fluence when IB mass density is set to $500\,amu/cm^3$ (i.e., Figure 7, red dashed line). The color of each line corresponds to the value of R_{O^+} used. As R_{O^+} increases from 0 to 100%, the net fluence is reduced by a factor of 16. Returning to the default IBC density and assuming 10% O^+ by number, the fluence at the end of the baseline simulation is reduced to 1.56×10^{26} ions/s. Assuming this moderate fraction of O^+, the default IB mass density remains a reasonable, if simple, approximation for real-world conditions.

This demonstration is also applicable to multispecies MHD [*Ma et al.*, 2002; *Glocer et al.*, 2009a], where there are several continuity equations but only one fluid momentum and energy equation. In a full multifluid approach, each species will accelerate independently, so the effect of changing R_{O^+} will not be as straight-forward. An initial investigation has been performed by *Winglee et al.* [2002], who found that large-scale features of fluence curves for both H^+ and O^+ are dependent on R_{O^+}.

Clearly, de facto fluxes are beholden to these two free parameters. While some initial work has been performed to set these parameters in a more realistic and dynamic manner [e.g., *Harnett et al.*, 2008], this appears to be a problem best addressed through the use of empirical or first-principles-based approaches. The de facto approach lacks causality between magnetosphere-ionosphere dynamics and the density and composition about the inner boundary.

The ability of the MHD model to drive fluxes that respond realistically to solar wind drivers with an ionospheric source that is only a static reservoir raises some fundamental questions. In these results, all radial acceleration occurs at magnetospheric altitudes (above $2.5\,R_E$ geocentric distance) as opposed to iono-spheric or "gap region" (within the MHD inner boundary) altitudes. Is sub-MHD acceleration negligible when attempting to account for ionospheric outflow effects on the global magnetosphere? Evidence to the con-trary can be found in *Glocer et al.* [2009a, 2009b] and *Welling et al.* [2011], which all demonstrated that the magnetospheric response is vastly different when a dynamic, first-principles-based outflow specification is imposed than when outflow is left to de facto mechanisms. Do these differences merely arise in differences in source populations, or does the imposed V_{radial} boundary condition from the outflow model play a strong role? The qualitative comparisons here represent a small first step in identifying similarities and resolving differences between de facto, physics-based, empirical, and real-world outflow.

Because the first step in the de facto outflow is numerical diffusion (at least when $V_{\text{radial}} = 0$), concerns may be raised over the role of numerics in this and other studies. This study represents the highest

near-boundary resolution simulation set amongst its peers ($\Delta \bar{x} = 0.0625\,R_E$, as opposed to $0.4\,R_E$ used by *Winglee* [1998, 2000], *Winglee et al.* [2002], and *Walker et al.* [2003], $0.25\,R_E$ used by *Harnett et al.* [2008], or $0.125\,R_E$ used by *Welling and Ridley* [2010a] and *Zhang et al.* [2007]), which should reduce diffusion substantially. However, the fluence values are all about the same order of magnitude for corresponding IB densities. One reason for this is that numerical diffusion acts on many variables, not just density. To illustrate, if the baseline simulation is repeated using the lower resolution of *Welling and Ridley* [2010a], the total fluence is reduced by 50% (not shown). Steep gradients that would drive diffusion cannot build under this lower resolution, slowing the rate at which mass leaves the inner boundary. To illustrate, in this simulation, the maximum pressure gradient near the inner boundary is only 20% of the higher resolution value. In the opposite extreme, removing all diffusion of mass into the domain would shut down outflow, which would be an unrealistic result.

Finally, this study highlights a key limitation to the single-fluid approach. Streamline 1 illustrated in Figure 5 (red line) shows unrealistic cusp behavior. Rather than the ionospheric population counterstreaming with precipitating solar wind plasma, it reaches pressure equilibrium and comes to a stop. This is because the two populations cannot counterstream because there is one fluid velocity for both. The ionospheric population is forced back earthward and eventually reaccelerates outward as if it had originated from postcusp latitudes. This behavior manifests as the "up-down-up" fluxes in Figures 2, 10, and 13 and may be inhibiting contributions from the dayside regions. Conversely, the solar wind population is shielded from the deep cusp, preventing any over-the-pole entry into the plasma sheet. Rectifying this cusp flow anomaly requires a multifluid approach that segregates all ionospheric populations from the solar wind fluid.

Overall, de facto-type outflow acts as a basic but reasonably realistic source of ionospheric plasma. The variability resulting from two free parameters (inner boundary mass density and composition) remain an issue which is currently best addressed by using either physics-based or empirical models to set the boundary conditions in a more dynamic and meaningful way. There are still many issues outstanding in terms of validating this source and determining the extent to which it deviates from other outflow specifications. However, as a means to obtain an ionospheric source of magnetospheric plasma, it requires zero additional user effort and captures large-scale characteristics successfully.

References

Axford, W. I. (1968), The polar wind and the terrestrial helium budget, *J. Geophys. Res.*, *73*, 6855–6859, doi:10.1029/JA073i021p06855.

Axford, W. I., and C. O. Hines (1961), A unifying theory of high-latitude geophysical phenomena and geomagnetic storms, *Can. J. Phys.*, *39*(10), 1433–1464.

Banks, P. M., and T. E. Holzer (1968), The polar wind, *J. Geophys. Res.*, *73*, 6846–6854, doi:10.1029/JA073i021p06846.

Barakat, A. R., and R. W. Schunk (1983), O^+ ions in the polar wind, *J. Geophys. Res.*, *88*(A10), 7887–7894, doi:10.1029/JA088iA10p07887.

Barakat, A. R., H. G. Demars, and R. W. Schunkm (1998), Dynamic features of the polar wind in the presence of hot magnetospheric electrons, *J. Geophys. Res.*, *103*(A12), 29,289–29,303, doi:10.1029/98JA02827.

Boris, J. P. (1970), A physically motivated solution of the Alfvén problem. *Tech. Rep. NRL Memorandum Report 2167*, Naval Research Laboratory, Washington, D. C.

Boynton, R. J., M. A. Balikhin, S. A. Billings, H. L. Wei, and N. Ganushkina (2011), Using the NARMAX OLS-ERR algorithm to obtain the most influential coupling functions that affect the evolution of the magnetosphere, *J. Geophys. Res.*, *116*(A5), A05218, doi:10.1029/2010JA015505.

Brambles, O. J., W. Lotko, P. A. Damiano, B. Zhang, M. Wiltberger, and J. Lyon (2010), Effects of causally driven cusp O^+ outflow on the storm time magnetosphere-ionosphere system using a multifluid global simulation, *J. Geophys. Res.*, *115*, A00J04, doi:10.1029/2010JA015469.

Brambles, O. J., W. Lotko, B. Zhang, M. Wiltberger, J. Lyon, and R. J. Strangeway (2011), Magnetosphere sawtooth oscillations induced by ionospheric outflow, *Science*, *332*(6034), 1183–1186, doi:10.1126/science.1202869.

Burke, W. J., M. C. Kelley, R. C. Sagalyn, M. Smiddy, and S. T. Lai (1979), Polar cap electric field structures with a northward interplanetary magnetic field, *Geophys. Res. Lett.*, *6*, 21–24.

Chappell, C. R., T. E. Moore, and J. H. Waite Jr. (1987), The ionosphere as a fully adequate source of plasma for the Earth's magnetosphere, *J. Geophys. Res.*, *92*, 5896–5910.

Chaston, C. C., J. W. Bonnell, C. W. Carlson, J. P. McFadden, R. E. Ergun, R. J. Strangeway, and E. J. Lund (2004), Auroral ion acceleration in dispersive Alfvén waves, *J. Geophys. Res.*, *109*, A04205, doi:10.1029/2003JA010053.

Chaston, C. C., C. W. Carlson, J. P. McFadden, R. E. Ergun, and R. J. Strangeway (2007), How important are dispersive Alfvén waves for auroral particle acceleration?, *Geophys. Res. Lett.*, *34*, L07101, doi:10.1029/2006GL029144.

Cladis, J. B. (1986), Parallel acceleration and transport of ions from polar ionosphere to plasma sheet, *Geophys. Res. Lett.*, *13*, 893–896, doi:10.1029/GL013i009p00893.

Cully, C. M., E. Donovan, A. W. Yau, and G. G. Arkos (2003), Akebono/Suprathermal Mass Spectrometer observations of low-energy ion outflow: Dependence on magnetic activity and solar wind conditions, *J. Geophys. Res.*, *108*(A2), 1093, doi:10.1029/2001JA009200.

Daglis, I. A., R. M. Thorne, W. Baumjohann, and S. Orsini (1999), The terrestrial ring current: Origin, formation, and decay, *Rev. Geophys.*, *37*, 407–438, doi:10.1029/1999RG900009.

Damiano, P. A., O. J. Brambles, W. Lotko, B. Zhang, M. Wiltberger, and J. Lyon (2010), Effects of solar wind dynamic pressure on the ionospheric O^+ fluence during the 31 August 2005 storm, *J. Geophys. Res.*, *115*, A00J07, doi:10.1029/2010JA015583.

De Zeeuw, D. L., T. I. Gombosi, C. P. T. Groth, K. G. Powell, and Q. F. Stout (2000), An adaptive MHD method for global space weather simulations, *IEEE Trans. Plasma Sci.*, *28*, 1956–1965.

Denton, M. H., M. F. Thomsen, H. Korth, S. Lynch, J. C. Zhang, and M. W. Liemohn (2005), Bulk plasma properties at geosynchronous orbit, *J. Geophys. Res.*, *110*(A9), A07223, doi:10.1029/2004JA010861.

Gagne, J. (2005), Implementation of ionospheric outflow in the LFM global MHD magnetospheric simulation, Master's thesis, Darthmouth College, Hanover, NH, U. S.

Ganguli, S. B. (1996), The polar wind, *Rev. Geophys.*, *34*, 311–348, doi:10.1029/96RG00497.

Garcia, K. S., V. G. Merkin, and W. J. Hughes (2010), Effects of nightside O$^+$ outflow on magnetospheric dynamics: Results of multifluid MHD modeling, *J. Geophys. Res.*, *115*, A00J09, doi:10.1029/2010JA015730.

Glocer, A., G. Tóth, T. Gombosi, and D. T. Welling (2009a), Modeling ionospheric outflows and their impact on the magnetosphere, initial results, *J. Geophys. Res.*, *114*, A05216, doi:10.1029/2009JA014053.

Glocer, A., G. Tóth, T. Ma, Y. Gombosi, J. Zhang, and L. Kistler (2009b), Multi-fluid BATS-R-US: Magnetospheric composition and dynamics during geomagnetic storms, initial results, *J. Geophys. Res.*, *114*, A12203, doi:10.1029/2009JA014418.

Gombosi, T. I., D. L. De Zeeuw, C. P. T. Groth, K. G. Powell, and P. Song (1998), The length of the magnetotail for northward IMF: Results of 3D MHD simulations, in *Physics of Space Plasmas*, vol. 15, edited by T. Chang and J. R. Jasperse, pp. 121–128, MIT Press, Cambridge, Mass.

Gombosi, T. I., G. Tóth, D. L. De Zeeuw, K. C. Hansen, K. Kabin, and K. G. Powell (2002), Semi-relativistic magnetohydrodynamics and physics-based convergence acceleration, *J. Comput. Phys.*, *177*, 176–205.

Guglielmi, A., J. Kangas, K. Mursula, T. Pikkarainen, O. Pokhotelov, and A. Potapov (1996), Pc 1 induced electromagnetic lift of background plasma in the magnetosphere, *J. Geophys. Res.*, *101*(A10), 21,493–21,500, doi:10.1029/96JA01750.

Harnett, E. M., R. M. Winglee, A. Stickle, and G. Lu (2008), Prompt ionospheric/magnetospheric responses 29 October 2003 Halloween storm: Outflow and energization, *J. Geophys. Res.*, *113*(A6), A06209, doi:10.1029/2007JA012810.

Horwitz, J. L. (1987), Core plasma in the magnetosphere, *Rev. Geophys.*, *25*, 579–587.

Horwitz, J. L., C. W. Ho, H. D. Scarbro, G. R. Wilson, and T. E. Moore (1994), Centrifugal acceleration of the polar wind, *J. Geophys. Res.*, *99*(A8), 15,051–15,064, doi:10.1029/94JA00924.

Lennartsson, O. W., H. L. Collin, and W. K. Peterson (2004), Solar wind control of Earth's H$^+$ and O$^+$ outflow rates in the 15-eV to 33-keV energy range, *J. Geophys. Res.*, *109*(A12), A12212, doi:10.1029/2004JA010690.

Lennartsson, W., and E. G. Shelley (1986), Survey of 0.1- to 16-keV/e plasma sheet ion composition, *J. Geophys. Res.*, *91*, 3061–3076.

Lyon, J., J. Fedder, and C. Mobarry (2004), The Lyon-Fedder-Mobarry (LFM) global MHD magnetospheric simulation code, *J. Atmos. Sol. Terr. Phys.*, *66*, 1333–1350.

Ma, Y., A. F. Nagy, K. C. Hansen, D. L. De Zeeuw, T. I. Gombosi, and K. Powell (2002), Three-dimensional multispecies MHD studies of the solar wind interaction with Mars in the presence of crustal fields, *J. Geophys. Res.*, *107*(A10), 1282, doi:10.1029/2002JA009293.

Moore, T., W. K. Peterson, C. T. Russell, M. O. Chandler, M. R. Collier, H. L. Collin, P. D. Craven, R. Fitzenreiter, B. L. Giles, and C. J. Pollock (1999), Ionospheric mass ejection in response to a CME, *Geophys. Res. Lett.*, *26*, 2339–2342.

Moore, T. E., and D. C. Delcourt (1995), The geopause, *Rev. Geophys.*, *33*, 175–210, doi:10.1029/95RG00872.

Moore, T. E., et al. (1997), High-altitude observations of the polar wind, *Science*, *277*(5324), 349–351, doi:10.1126/science.277.5324.349.

Morley, S. K., J. Koller, D. T. Welling, and B. A. Larsen (2010), Spacepy—A Python-based library of tools for the space sciences, in *Proceedings of the 9th Python in Science Conference*, edited by S. van der Walt and J. Millman, pp. 39–45, Los Alamos National Laboratory (LANL), N. M.

Nosé, M., R. W. McEntire, and S. P. Christon (2003), Change of the plasma sheet ion composition during magnetic storm development observed by the Geotail spacecraft, *J. Geophys. Res.*, *108*, 1201, doi:10.1029/2002JA009660.

Ouellette, J. E., O. J. Brambles, J. G. Lyon, W. Lotko, and B. N. Rogers (2013), Properties of outflow-driven sawtooth substorms, *J. Geophys. Res. Space Physics*, *118*(6), 3223–3232, doi:10.1002/jgra.50309.

Powell, K., P. Roe, T. Linde, T. Gombosi, and D. L. De Zeeuw (1999), A solution-adaptive upwind scheme for ideal magnetohydrodynamics, *J. Comput. Phys.*, *154*, 284–309.

Ridley, A., T. Gombosi, and D. L. De Zeeuw (2004), Ionospheric control of the magnetospheric configuration: Conductance, *Ann. Geophys.*, *22*, 567–584.

Ridley, A. J., K. C. Hansen, G. Tóth, D. L. De Zueew, T. I. Gombosi, and K. G. Powell (2002), University of Michigan MHD results of the GGCM metrics challenge, *J. Geophys. Res.*, *107*(A10), 1290, doi:10.1029/2001JA000253.

Ridley, J. A., and M. W. Liemohn (2002), A model-derived storm time asymmetric ring current driven electric field description, *J. Geophys. Res.*, *107*(A8), 1151, doi:10.1029/2001JA000051.

Rusanov, V. (1961), Calculation of interaction of non-steady shock waves with obstacles, *JJ. Comput. Math. Phys.*, *1*, 267–279.

Siscoe, G. L., G. M. Erickson, B. U. O. Sonnerup, N. C. Maynard, K. D. Siebert, D. R. Weimer, and W. W. White (2001), Relation between cusp and mantle in MHD simulation, *J. Geophys. Res.*, *106*(A6), 10,743, doi:10.1029/2000JA000385.

Tóth, G., D. L. D. Zeeuw, T. I. Gombosi, W. B. Manchester, A. J. Ridley, I. V. Sokolov, and I. I. Roussev (2007), Sun to thermosphere simulation of the October 28–30, 2003 storm with the Space Weather Modeling Framework, *Space Weather*, *5*, S06003, doi:10.1029/2006SW000272.

Walker, R. J., M. Ashour-Abdalla, T. Ogino, V. Peroomian, and R. L. Richard (2003), Modeling magnetospheric sources, in *Earth's Low-Latitude Boundary Layer, Geophys. Monogr. Ser.,* vol. 133, edited by P. T. Newell and T. Onsager, pp. 33–43, AGU, Washington, D. C., doi:10.1029/133GM03.

Wang, H., A. J. Ridley, and H. Luhr (2008), Validation of the Space Weather Modeling Framework using observations from CHAMP and DMSP, *Space Weather*, *6*, S03001, doi:10.1029/2007SW000355.

Welling, D. T., and A. J. Ridley (2010a), Exploring sources of magnetospheric plasma using multispecies MHD, *J. Geophys. Res.*, *115*(A14), A04201, doi:10.1029/2009JA014596.

Welling, D. T., and A. J. Ridley (2010b), Validation of SWMF magnetic field and plasma, *Space Weather*, *8*, S03002, doi:10.1029/2009JA014596.

Welling, D. T., V. K. Jordanova, S. G. Zaharia, A. Glocer, and G. Toth (2011), The effects of dynamic ionospheric outflow on the ring current, *J. Geophys. Res.*, *116*, A00J19, doi:10.1029/2010JA015642.

Wiltberger, M., W. Lotko, J. G. Lyon, P. Damiano, and V. Merkin (2010), Influence of cusp O$^+$ outflow on magnetotail dynamics in a multifluid MHD model of the magnetosphere, *J. Geophys. Res.*, *115*, A00J05, doi:10.1029/2010JA015579.

Winglee, R. M. (1998), Multi-fluid simulations of the magnetosphere: The identification of the geopause and its variation with IMF, *Geophys. Res. Lett.*, *25*, 4441–4444.

Winglee, R. M. (2000), Mapping of ionospheric outflows into the magnetosphere for varying IMF conditions, *J. Atmos. Sol. Terr. Phys.*, *62*, 527–540.

Winglee, R. M. (2003), Circulation of ionospheric and solar wind particle populations during extended southward interplanetary magnetic field, *J. Geophys. Res.*, *108*, 1385, doi:10.1029/2002JA009819.

Winglee, R. M., D. Chua, M. Brittnacher, G. K. Parks, and G. Lu (2002), Global impact of ionospheric outflows on the dynamics of the magnetosphere and cross-polar cap potential, *J. Geophys. Res.*, *107*, 1237, doi:10.1029/2001JA000214.

Winglee, R. M., W. K. Peterson, A. W. Yau, E. Harnett, and A. Stickle (2008), Model/data comparisons of ionospheric outflow as a function of invariant latitude and magnetic local time, *J. Geophys. Res.*, *113*, A06220, doi:10.1029/2007JA012817.

Yau, A., and M. André (1997), Sources of ion outflow in the high latitude ionosphere, *Space Sci. Rev.*, *80*, 1–25.

Yau, A. W., W. K. Peterson, and E. G. Shelley (1988), Quantitative parametrization of energetic ionospheric ion outflow, in *Modeling Magnetospheric Plasma, Geophys. Monogr. Ser.*, vol. 44, edited by T. E. Moore and J. H. Waite Jr., pp. 211–217, AGU, Washington D. C.

Yu, Y., and A. J. Ridley (2008), Validation of the space weather modeling framework using ground-based magnetometers, *Space Weather*, *6*, S05002, doi:10.1029/2007SW000345.

Yu, Y., and A. J. Ridley (2013), Exploring the influence of ionospheric O^+ outflow on magnetospheric dynamics: Dependence on the source location, *J. Geophys. Res. Space Physics*, *118*, 1711–1722, doi:10.1029/2012JA018411.

Zhang, J., et al. (2007), Understanding storm-time ring current development through data-model comparisons of a moderate storm, *J. Geophys. Res.*, *112*, A04208, doi:10.1029/2006JA011846.